Electronically swept millimetre-wave interferometer for spatially resolved measurement of plasma electron density

John Howard and David Oliver

Plasma Research Laboratory, Research School of Physical Sciences and Engineering, Australian National University, Canberra, ACT, 0200, Australia

john.howard@anu.edu.au

We report the development and initial implementation of a new rapid-spatial-scan millimetre-wave interferometer for plasma density measurements. The fast scan is effected by electronic frequency sweeping of a wide-band (180-280GHz) backward-wave oscillator (BWO) whose output is focussed onto a fixed blazed diffraction grating. The system, which augments the rotating-grating scanned multi-view H-1 heliac interferometer can sweep the plasma cross-section in a period less than 1 ms with a beam diameter in the plasma of 20mm and phase noise of order 0.01 radians.

OCIS codes: 120.3180

1. Introduction

Measurement of the two-dimensional plasma electron density distribution is essential for understanding the properties of magnetically confined fusion plasmas. The electron number density is usually estimated from the interferometrically measured phase shift imparted on a probing far-infrared laser or microwave beam [1, 2]. In many plasma devices this is achieved by using a number of discrete beams [3] or, when access allows, by imaging a laser beam expanded to illuminate a significant portion of the plasma cross-section [4, 5]. The cost for such systems increases with the number of spatial channels. Spatially scanning the plasma [6, 7] effectively reduces the interferometric system to a single chord, thereby maximizing the available power probing the plasma and reducing system cost.

The H-1 heliac, located in the Plasma Research Laboratory at the Australian National University, is a flexible, medium scale helical-axis stellarator. The device is constructed with its magnetic coil set enclosed inside a 4m diameter vacuum tank. The coil-in-tank construction allows almost unhindered diagnostic access to the plasma cross-section. To take

advantage of this, we have constructed a spatially scanning far-infrared interferometer that provides multiple projections of the plasma region to facilitate tomographic reconstruction of the plasma density contours from the measured interferometric phase shifts.

The interferometer uses a rotating cylindrical diffraction grating to rapidly mechanically sweep the laser beam across the plasma region in three distinct viewing directions. This is achieved by scribing the circumference of the rotating wheel (~ 350 mm diameter) with a grating pattern whose groove spacing d varies with wheel rotation angle either continuously or in small discrete steps. Rotation of the wheel generates a fan of diffracted beams that can be focused and directed into the plasma region. The rotation also generates a Doppler frequency offset of the probing beams that conveniently allows for heterodyne detection of the plasma produced phase shift.

The interferometer, which is configured in a Michelson arrangement, is fed by an optically pumped (80W, 10.6 μm) far-infrared (FIR) laser that can produce useful output power at a number of discrete wavelengths between $\lambda = 100\,\mu$m and $\lambda = 1000\,\mu$m The laser-based interferometer is adequate for high plasma densities, but suffers signal to noise ratio problems at lower densities, and is unable to temporally resolve fast plasma changes such as particle confinement transitions and the onset of instability.

The advent of relatively inexpensive electronically tunable wide-band (180-280 GHz) cw high power (20-100 mW) backward wave oscillators (BWO) [8] has suggested the possibility of combining a wide-band frequency sweep and a diffraction grating to effect both a rapid and electronically programmable spatial plasma scan. We report the development and installation of a rapid electronically-swept, high-sensitivity millimetre-wave interferometer for plasma electron density measurements on the H-1 heliac. Requiring no moving parts, the BWO-based system is mechanically quiet, compact and robust, and is capable of producing a 500mm spatial scan of the plasma in $\lesssim 100\mu$s. To the authors' knowledge, the use of an electronically controlled source frequency to effect a spatial scan has not previously been employed in millimetre-wave interferometry.

This paper is organized as follows. Section 2 gives a brief overview of the existing scanning multi-view interferometer with some emphasis on its limitations. In Sec. 3 we introduce ELSI, the electronically scanned interferometer, and summarize the various competing design considerations. In Sec. 4 we report imaging experiments on a variety of phase targets using a prototype bench-top system that illustrate the achievable phase, temporal and spatial resolution. We also describe the new numerical methods which have been developed for demodulation of the complicated interference fringe patterns. The installation on the H-1 heliac is discussed briefly in Sec. 5 and first plasma results presented.

2. Overview of the H-1 multi-view scanning interferometer

For a two beam interferometer, the detected interferometer signal is given by

$$S(t) = I(t)\left[1 + \zeta(t)\cos\phi(t)\right] \tag{1}$$

where $I(t)$ is the possibly time dependent intensity of the combined probe and local oscillator beams, $\zeta(t)$ is the fringe contrast and $\phi(t)$ is the phase shift between the interferometer arms. The propagation phase shift in a given arm is given by

$$\varphi = \frac{2\pi\nu}{c}\int_0^L \mu(\nu,t)\mathrm{d}l \tag{2}$$

where ν is the probing radiation frequency and $\mu(\nu,t)$ is the refractive index. For ordinary mode propagation in plasma the refractive index is given by [9]

$$\mu = \left(1 - \frac{\nu_{\mathrm{pe}}^2}{\nu^2}\right)^{1/2} \tag{3}$$

where

$$\nu_{\mathrm{pe}} = \left(\frac{n_{\mathrm{e}}e^2}{4\pi^2 m_{\mathrm{e}}\epsilon_0}\right)^{1/2} \tag{4}$$

is the plasma frequency and n_{e} is the electron number density. When the probing frequency is sufficiently high, the plasma-induced phase shift is given by the approximate formula

$$\varphi_P(t) = r_{\mathrm{e}}\lambda\int_0^{L_p} n_{\mathrm{e}}\mathrm{d}l \tag{5}$$

where r_{e} is the classical electron radius, L_p is the length of the plasma path and λ is the instantaneous source wavelength. To obtain spatially resolved density information it is necessary to make many line integrated plasma density measurements and apply suitable inverse methods.

The H-1 interferometer presently uses a rotating diffraction grating to generate the required plasma spatial scan. For radiation of wavelength λ incident at angle α onto a grating of groove spacing d, the mth order diffraction angle β is given by

$$\sin\alpha + \sin\beta = \frac{m\lambda}{d}. \tag{6}$$

For fixed α, and operating in first order ($m = 1$), one can vary d either continuously or in discrete steps to generate a span of diffraction angles $\Delta\beta = 12^\circ$. The groove pattern can be replicated around the circumference to produce a number of plasma sweeps per wheel rotation. Temporal resolution is limited by the maximum grating rotation speed 6000 rpm which, for six plasma sweeps per rotation, gives a minimum plasma sweep time of $\sim$ 2ms. At the center of the plasma the probe beam has a full width at half maximum of $\sim$ 20mm.

By illuminating the wheel from different directions it is possible to generate diffracted beams that probe the plasma at multiple view angles as seen in the Gaussian ray trace simulation [10] shown in Fig. 1. The support structure for the internal mirrors is connected to the external vibration-isolated table via rods passing through flexible vacuum bellows. In each view, the interferometer uses one beam polarization component to probe the plasma and the other in a reference interferometer to monitor wheel vibrations.

The wheel rotation conveniently Doppler shifts the probing beam frequency by up to 500 kHz to allow heterodyne detection of the phase modulated radiation. The interferograms are digitized directly and the phase demodulation is performed numerically post-shot. A Fourier shifting algorithm is used to correct for the non-simultaneous spatial sampling due to the scanning nature of the interferometer. The continuously sampled projection is then binned into a preset number of channels chosen to obtain a satisfactory trade-off between spatial resolution and signal to noise ratio. The system achieves rms noise levels of around 0.01 radians compared to a plasma induced phase shift of up to 3.5 radians.

The FIR laser operating wavelength is a compromise between available output power (decreases with λ), total phase shift (proportional to λ) and mechanical phase noise ($\sim \lambda^{-1}$). While laser source power at wavelength $\lambda = 433\,\mu$m (40 mW) delivers adequate detector SNR for the multi-view system, the measured phase shifts are also more susceptible to vibration-induced phase noise, especially when probing the low-density plasma edge regions. Some of this noise is coupled from the vibration of the grating motor drive, and is difficult to eliminate entirely. To reduce this vibrational noise component, the laser can be operated at $\lambda = 743\,\mu$m but with lower output power (10 mW) and poorer overall SNR when feeding all views. Use of the BWO alleviates these problems by providing higher power at the longer wavelengths that are more sensitive to the plasma.

To illustrate the rotating grating interferometer performance, while also drawing attention to certain limitations, we show some example projection data (Fig. 2) for a discharge in argon that collapses to a strong oscillating global instability (bottom). The figure juxtaposes information from the two diagonal views (projections). The temporal undersampling of the global oscillation produces Moiré fringe patterns.

3. ELSI - Electronically scanned interferometer

To allow the H-1 interferometer to attain its full tomographic imaging capability, we have installed a high power (100 mW) voltage tunable 180-280 microwave BWO tube as a radiation source for an electronically scanned interferometer that now replaces the central horizontal view of the existing H-1 grating-scanned interferometer.

Illuminating a static blazed grating ($m = 1$, $d = 1.33\,$mm, $\alpha = 52^\circ$) and sweeping the frequency from 220-270 GHz generates a similar range of diffraction angles β as currently

produced by the rotating scanning grating. The operating principle of the new interferometer is illustrated in Fig. 3. The spatial sweep is arranged so that the probe wavelength decreases (sensitivity to plasma density increases) as the scan moves from plasma centre to edge.

The source frequency is swept in an approximately linear fashion by applying a periodic ramp control signal ($\sim 4-6$V) that is internally amplified by the BWO power supply and applied to the tube cathode. The path difference between the probing and local oscillator beams gives rise to a small time delay $\tau = \Delta L/c$ (and hence frequency difference) between the wave fronts arriving at the detector, allowing for heterodyne detection of the plasma phase shift. A similar approach is used in standard chirped-frequency interferometry where the amplitude of the applied sawtooth frequency sweep is adjusted so as to produce a single cycle of the carrier wave per period of the modulating sawtooth ramp [11].

The instantaneous frequency of the BWO is a function of the applied cathode voltage $\nu = \nu(V)$. For a fixed frequency ν_0 the microwave phase varies linearly in time $\varphi(t) = 2\pi\nu_0 t$ and the interferometric phase difference is constant: $\phi(t) \equiv \varphi(t+\tau) - \varphi(t) = 2\pi\nu_0\tau$. For an applied voltage waveform $V(t)$, the rate of change of phase difference gives rise to a carrier signal whose intermediate frequency (IF) is given by

$$f_{\rm IF} = \frac{1}{2\pi}\frac{{\rm d}\phi}{{\rm d}t} = \tau\frac{{\rm d}\nu}{{\rm d}\tau} = \tau\frac{{\rm d}\nu}{{\rm d}V}\frac{{\rm d}V}{{\rm d}t}. \tag{7}$$

For a periodic sawtooth voltage ramp, the interferometer sweeps through a fixed number of waves (per ramp period)

$$N = \Delta\nu\frac{\Delta L}{c} \tag{8}$$

which depends only on the path difference ΔL and the range of the frequency sweep $\Delta\nu = [\nu(V_2) - \nu(V_1)]$. The instantaneous interference fringe frequency depends on the details of the voltage dependence of the output millimetre-wave frequency $\nu(V)$ as well as the applied voltage ramp period T. The instantaneous interferometer phase (see Equation 1) is then given by $\phi(t) = 2\pi f_{\rm IF}t + \varphi_P(t)$ and the plasma produced phase shift can be recovered by monitoring the carrier frequency phase using a second reference interferometer.

3.A. Interferometer design considerations

The overall aim is to construct an interferometer that gives a useful compromise between spatial resolution R in the plasma (small spot size, wide sweep bandwidth) and time resolution (high scan rate, smaller sweep bandwidth, low N). The achievable spatial resolution R in the plasma region is given by the ratio of the width $W = F\Delta\beta \sim mF\Delta\lambda/d\cos\bar{\beta}$ of the scanned plasma region after the first collimating optic (parabola of focal length F) to the diameter $w = \lambda F/\pi w_0$ of the beam spot at distance F after the parabola. Here $\bar{\beta}$ is the mean diffraction angle and w_0 is the beam spot diameter (defined here to be twice the radius

of the $1/e$ point of the beam power profile) on the grating. We find

$$R = \frac{m\pi}{\cos\bar{\beta}} \frac{w_0}{d} \frac{\Delta f}{f} \tag{9}$$

The requirement that the beam be well collimated also requires that the Rayleigh length $z_R = \pi w^2/2\lambda$ be greater than the plasma dimension a, and this sets a maximum limit on the system resolution. Thus, taking $a \sim W$, it is easy to show that $R_{\max} \sim \sqrt{a/\lambda}$.

There are several competing constraints on the choice of the frequency sweep range. Firstly, $\Delta\nu$ must be chosen in conjunction with the diffraction grating to generate the range of diffraction angles required to spatially scan the plasma region. A wide frequency range gives higher spatial resolution. On the other hand, due to the natural divergence of the mm-waves it is advantageous to restrict the sweep range to simplify beam focussing and collimation. A wide frequency sweep can also reduce the achievable interferometer scan rate due to the natural bandwidth limitations of the BWO power supply.

Both the BWO output power and the detection system response can also vary significantly with frequency. Reducing $\Delta\nu$ to minimize the effect of these variations, however, reduces the number of interference fringes N available per sweep to capture the plasma phase profile. It is therefore necessary to choose the path length difference ΔL such that the fringe period is significantly less than the period of typical amplitude variations. Figure 4, which shows an interferogram for a frequency sweep in the range of $220 - 270$ GHz indicates that $N \sim 200 - 400$ fringes per sweep are required. In our case then, we have taken $\Delta\nu/\nu \sim 0.12$, $w_0/d \sim 15$ and $\bar{\beta} = 22^\circ$ to obtain $R \sim 6$ compared with $R_{\max} \sim 10$.

Note that doubling the grating width and changing the blaze angle to favour second order diffraction (m/d stays approximately constant), can halve the required wavelength sweep range thereby reducing the sweep time and the effects of output power modulation. However, this also increases the beam spot size in the plasma and reduces the system spatial resolution. It should also be noted that the number of fringes N per sweep should be sufficient to resolve the R independent beam positions in the plasma region ($N > R$). The interferogram is clearly adequately sampled when $N \gtrsim 200$.

It is desirable to scan the plasma with high repetition rate. The bandwidth of the high voltage amplifier that supplies the cathode bias ultimately limits the achievable sweep rate. For the present system, this is set to ~ 10 kHz by output filter capacitors, and represents a compromise between tuning speed and output phase jitter introduced by noise on the applied cathode voltage. As discussed in section 4.A, we use an independent interferometer to monitor and accurately compensate this noise. For $N \sim 400$ waves and a 1kHz repetition rate, the intermediate frequency is of order $f_{\rm IF} = 400$ kHz and the required information bandwidth is $\Delta f \sim f_{\rm IF}/R$. The fringes can therefore be digitally acquired and demodulated post-shot.

4. Bench tests using a prototype interferometer

Extensive benchtop experiments were undertaken to test the ELSI principle, characterize its performance and to develop and test the demodulation algorithms required to extract the phase information. A schematic layout of the bench-top Michelson interferometer is presented in Fig. 3.

A periscope constructed of plane and paraboloidal mirrors is used to direct and collimate the BWO radiation into the interferometer. A wire-grid polarizer oriented with its wires at 45° to the incident vertically polarized beam splits half the radiation to a reference interferometer which is used to monitor the instantaneous interferometer phase. The transmitted component passes through a second polarizer with wires also oriented at 45° before being intercepted by a horizontal polarizer (grid oriented at 0°) that directs half the radiation to the diffraction grating (90% efficient for radiation polarized normal to the grooves) with the remainder to a fixed return mirror. The diffracted beam is collected and focussed by a parabolic mirror into the region nominally occupied by the plasma. Various test objects can be placed in this region to measure the system spatial, temporal and phase resolution.

For each interferometer, the returned, orthogonally polarized probe and local oscillator beams are combined via a polarizer and paraboloidal mirror onto horn-waveguide coupled broadband zero-biased Schottky diode detectors. An example of the detected signal for the probe interferometer during an applied linear voltage sweep is shown in Fig. 4. The half of the returned power directed back to the source can give rise to cross-talk problems between the various coupled interferometer arms. The interferometer arm lengths and separations are thus designed such that the additional path length traversed by multi-path beams conveniently shifts their associated IF carriers to distinct frequencies that can be subsequently removed by numerical filtering. This feature eliminates the need to isolate the interferometers using absorbers, and therefore results in a better signal to noise ratio for the probe beam signals.

4.A. Demodulation

The BWO output frequency is a monotonic but "bumpy" function of applied control voltage. For an applied linear ramp, and depending on the interferometer design, the IF frequency and amplitude can both vary substantially over a small number of fringe periods. In principle, the IF variations can be largely removed by applying an appropriate voltage waveform that compensates for this non-linearity. This has the additional advantage of maintaining an approximately constant number of sampling points per cycle and reducing the required detection electronics bandwidth. In practice, however, it is difficult to compensate for the filtering effects of the power supply cathode-voltage smoothing capacitors and this approach to signal regularization (i.e. constant IF) is limited to plasma sweep rates less than 100 Hz. The advantage of constant IF is that electronic phase-locked-loops can be applied for phase

demodulation of the IF carrier.

When the IF signal is not electronically demodulated, numerical techniques must be used to calculate the phase for both the digitized probe and reference waveforms. In this procedure, the waveforms are first amplitude normalized onto [-1,1]. An applied FFT is the used to calculate the analytic signal by zeroing negative frequency components and performing the inverse transform. An arctangent of the resulting complex signal returns the carrier phase evolution. The signal timebase is subsequently distorted using the measured phase variation in such a way as to produce an approximately constant intermediate frequency [see Fig. 5(a)]. This has the merit of allowing the isolation of multi-path crosstalk components which, by virtue of their differing optical path lengths, show up as separated peaks in the resulting power spectrum [see Fig. 5(b)]. The numerically phase regularized signal can be filtered to remove the crosstalk components, leaving the phase modulated primary carrier signal shown in Fig. 5(c). This signal is subsequently mapped back onto its original timebase. The procedure is applied to both probe and reference interferometers and, in the absence of a plasma or other phase object, their phase traces can be subtracted to provide a"vacuum" phase difference baseline. When the plasma is produced, this vacuum phase baseline can be subtracted from the difference between the probe and reference interferometers to obtain the nett plasma produced phase shift $\varphi_P(t)$.

Once crosstalk components have been removed, residual phase noise is due to vibrations (which are negligible in our case), detector noise and phase noise due to fluctuations in the instantaneous microwave source frequency. These fluctuations arise from noise on the applied cathode high voltage. Even in the absence of noise, an applied digital control voltage with 16 bit resolution in the control voltage sweep range will result in a phase uncertainty of $2\pi N/2^{16} \approx .04$ radians ($\sim 2^\circ$). The inevitable source phase jitter, which is the dominant noise source for the interferometer, can be monitored using a separate reference interferometer as shown in Fig. 3

4.B. Measurements of test phase objects

In order to establish the phase and spatial resolution of the ELSI system, mylar sheets of thickness $0.05 - 0.25$ mm and widths $5 - 40$ mm are used as test phase objects. These objects are placed in the "plasma" region shown in Figure 3 while the applied electronic ramp voltage sweeps the millimetre-wave beam across the object. The acquired interferograms are demodulated to obtain the object phase shift profile.

Figure 6 (a) shows the measured phase profiles of a 30 mm wide, 0.25 mm thick mylar target located at 4 equi-spaced positions in the interferometer sweep. The increase in phase shift with increasing distance coordinate is due to the change of probing wavelength across the sweep as well as wavelength-dependence of the object refractive index.

In Fig 6 (b) the phase shift profiles of objects with widths 5, 10, 20 and 40 mm are used to estimate the spatial resolution. The response is modeled by convolving a Gaussian profile with the rectangular target phase profiles. The best fit results, which are shown superimposed on the measured profiles indicate a beam diameter of ~ 20 mm in the plasma region. The discrepancy between the measured and modeled phase profiles is likely due to a slight misalignment in the probe beam. In a Michelson interferometer a misalignment will produce a broadened phase profile and will also affect the peak phase perturbation.

5. First plasma measurements

We report first measurements obtained on the H-1 heliac using ELSI. The interferometer configuration closely resembles the benchtop system shown in Fig. 3, and replaces the view of the bottom half of the plasma previously provided by the laser and scanning grating (see Fig. 1).

Because of the longer BWO probe wavelengths, it is necessary to assess the likely effects of refraction. The maximum angle of refraction for a cylindrical plasma having a parabolic density profile is given by [12]

$$\alpha_{\max} = \sin^{-1}(n_0/n_c) \approx 9 \times 10^{-16} n_0 \lambda^2 \tag{10}$$

where n_0 is the plasma peak density and n_c is the propagation cutoff density at which the probing frequency equals the plasma frequency (see Eq. 4). For H-1 experiments, the expected maximum displacement of a beam making a double pass of a plasma of central density $n_{e0} = 10^{18}\mathrm{m}^{-3}$ for $\lambda = 1.25$mm and at a distance $L = 2$ m from the plasma (see Fig. 3) is $2L\alpha_{max} \approx 6$mm and can be effectively ignored for the horizontal plasma view.

Figure 7 shows a sequence of phase profiles (density projections) for a typical 0.5 T radio-frequency heated hydrogen discharge in the standard heliac magnetic configuration. The ELSI frequency sweep range 220-270GHz was sufficient to span 20cm. The availability of high speed digitizers (2MHz) allows a scan repetition rate for plasma measurements of 500 s^{-1}. The data are presented in three different formats. Figure 7 (a) shows the demodulated interferogram raw time series. The multiple sweeps across the plasma appear as successive traces commencing near zero at the plasma bottom edge (longer wavelength) and climbing to a peak as the beam reaches the plasma centre (shorter wavelength). The traces have been corrected for the wavelength dependence of the interferometric phase shift (see Eq. 5) and are shown as an equivalent average plasma density normalized to the optical path length across the plasma centre. The noise level is 2% of the peak phase shift. In Fig. 7 (b), the data are rearranged into an array format indexed according to scan start time (horizontal axis) and spatial position in the plasma (vertical axis). The resulting contour plot gives a clearer representation of the spatio-temporal evolution of the density profile. Slices at fixed

spatial position have not been shifted by the associated small delay attending the temporal nature of the sweep. This correction could be simply implemented using a Fourier shifting algorithm.

Figure 8 presents the sequence of plasma profiles in a single graph. An artifact due to the presence of a seam in the internal return mirror is evident and the signal to noise ratio can be easily assessed. Following an initial uniform increase in plasma density, the edge density remains fixed while the mid-radius density gradient rises. The fixing of the edge density may be related to the nature of the minority-heating scheme and the close-proximity of the heating antenna to the plasma edge. Centrally electron-cyclotron heated discharges exhibit distinctly different profiles. These issues will be discussed in more detail in a future paper.

References

1. A. J. H. Donné, "High spatial resolution interferometry and polarimetry in hot plasmas," Rev. Sci. Instrum. **66**, 3407–3423 (1995).
2. H. J. Hartfuss, T. Geist, and M. Hirsch, "Heterodyne methods in millimetre wave plasma diagnostics with applications to ECE, interferometry and reflectometry," Plasma Physics and Controlled Fusion **39**, 1693–1769 (1997).
3. K. Kawahata, K. Tanaka, and Y. Ito, "Far infrared laser interfereometer system on the Large Helical Device," Rev. Sci. Instrum. **70**, 707–709 (1999).
4. Y. Jiang and D. Brower, "Horizontal-view interferometer on TEXT-Upgrade," Rev. Sci. Instrum. **66**, 852–854 (1995).
5. J. H. Rommers, A. J. H. Donné, F. A. Karelse, and J. Howard, "The multichannel triple-laser interferometer/polarimeter system at RTP," Rev. Sci. Instrum. **68**, 1217–1226 (1997).
6. J. Howard, "Novel Scanning Interferometer for Two-Dimensional Plasma Density Measurements," Rev. Sci. Instrum. **61**, 1086–1094 (1990).
7. G. Warr, B. D. Blackwell, J. Wach, and J. Howard, "First Results from the Three View Far-infrared Interferometer for the H-1 Heliac," Fusion Eng. And Design **34-35**, 387–391 (1997).
8. ELVA-1. 46 Robezu, LV-1004, Riga, Latvia.
9. I. H. Hutchinson, *Principles of Plasma Diagnostics* (Cambridge University Press, Cambridge, 1987).
10. G. Warr and J. Howard, "grt3d: A three-dimensional gaussian-beam ray-tracing program for designing interferometer/polarimeter plasma diagnostics," Rev. Sci. Instrum. **72**, 2305–2309 (2001).
11. L. Porte, C. L. Rettig, W. A. Peebles, and X. Nguyen, "Design and operation of a low cost, reliable millimeter-wave interferometer," Rev. Sci. Instrum. **70**, 1082–84 (1999).
12. D. Véron, "Submillimeter Interferometry of High Density Plasmas," in *Infrared and Millimeter Waves*, K. Button, ed., vol. 2, pp. 69–135 (Academic Press, New York, 1979).

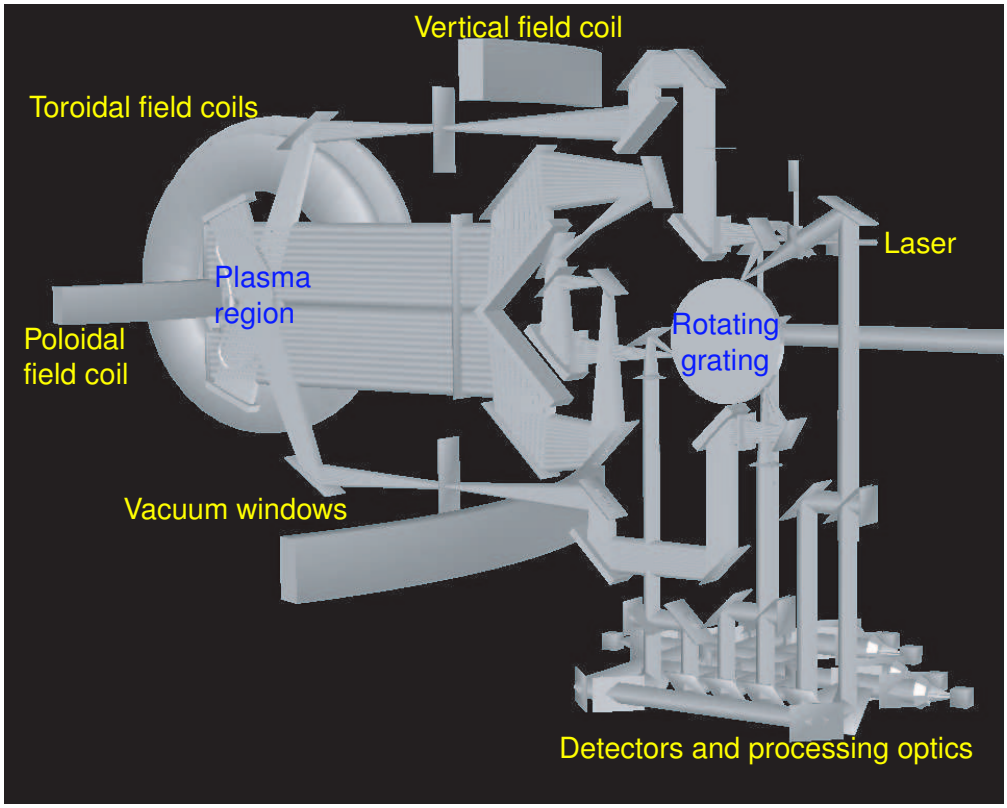
Vertical field coil
Toroidal field coils
Laser
Plasma
region
Rotating
grating
Poloidal
field coil
Vacuum windows
Detectors and processing optics

Fig. 1.

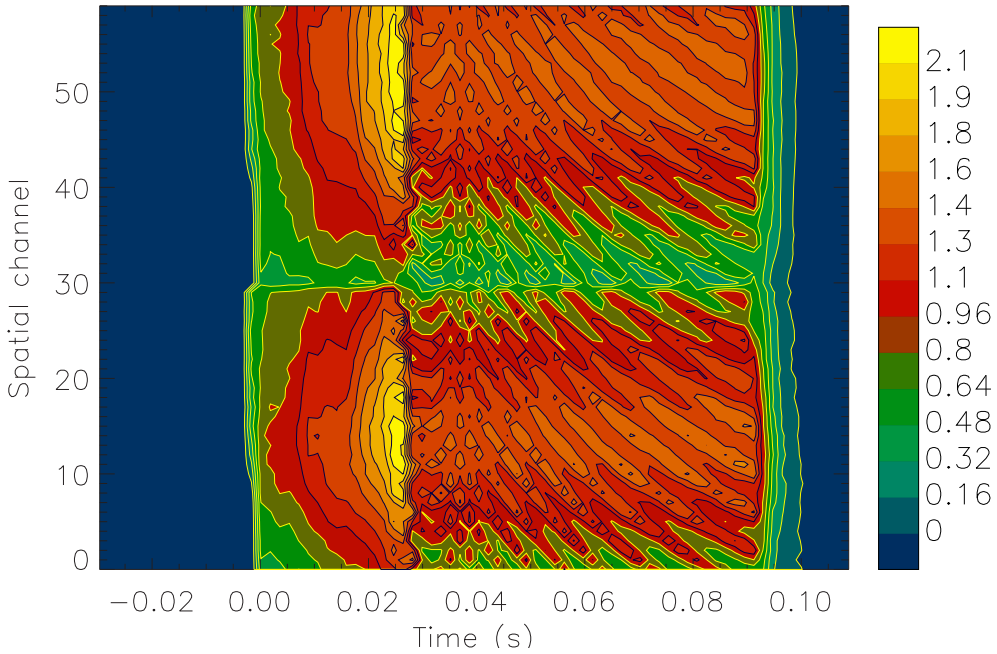
Spatial channel
50
40
30
20
10
0
−0.02
0.00
0.02
0.04
0.06
0.08
0.10
Time (s)
2.1
1.9
1.8
1.6
1.4
1.3
1.1
0.96
0.8
0.64
0.48
0.32
0.16
0

Fig. 2.

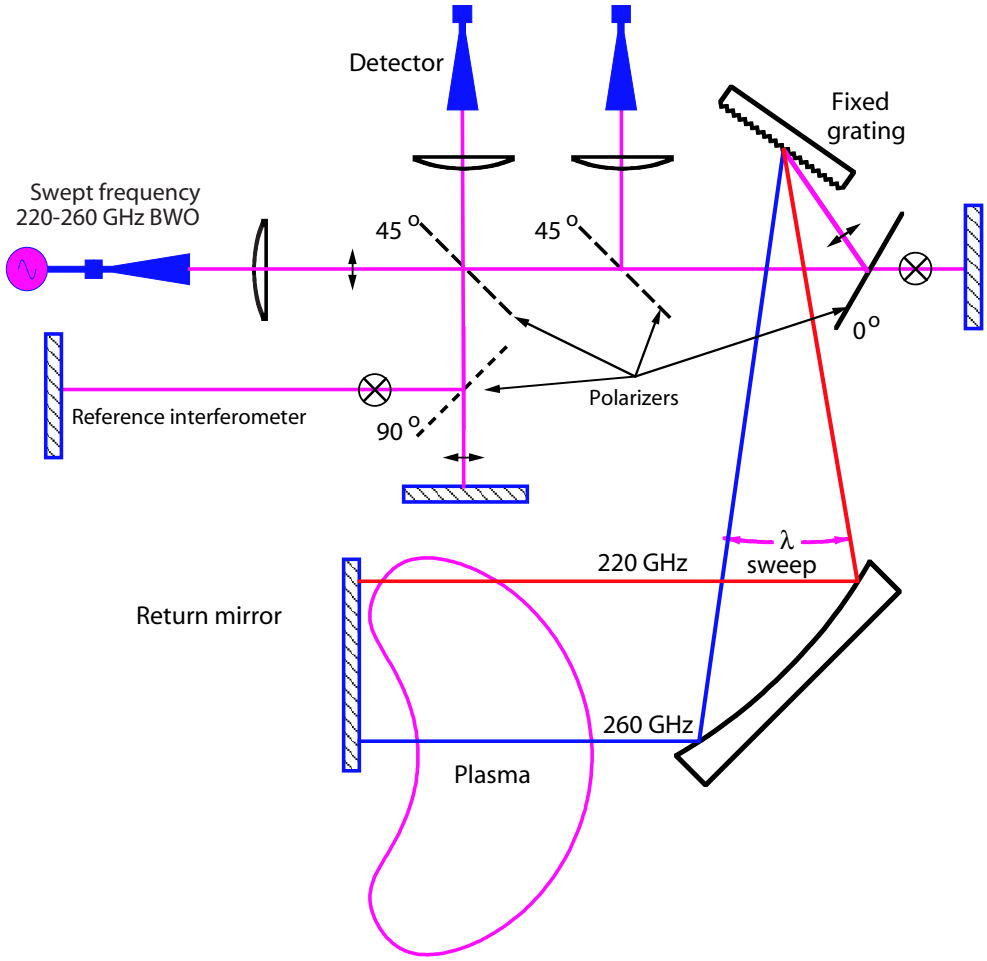
Detector
Fixed
grating
Swept frequency
220-260 GHz BWO
45 °
45 °
0°
Reference interferometer
90 °
Polarizers
λ
sweep
220 GHz
Return mirror
260 GHz
Plasma

Fig. 3.

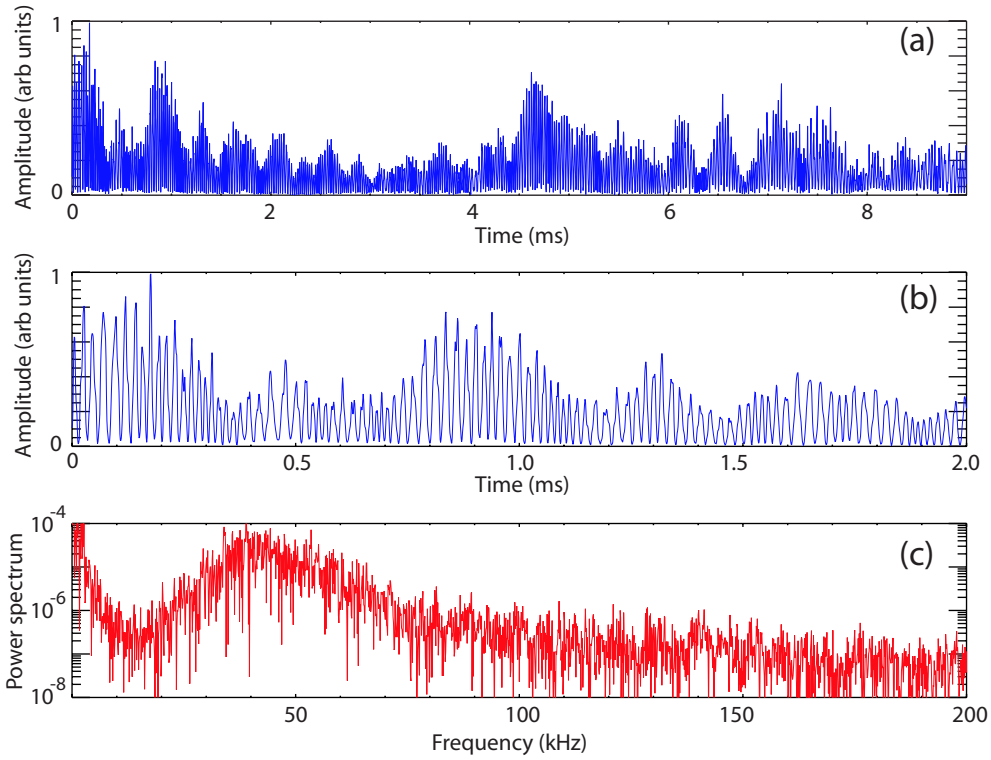
Amplitude (arb units)
1
0
(a)
0
2
4
6
8
Time (ms)
Amplitude (arb units)
1
0
(b)
0
0.5
1.0
1.5
2.0
Time (ms)
Power spectrum
10^-4
10^-6
10^-8
(c)
50
100
150
200
Frequency (kHz)

Fig. 4.

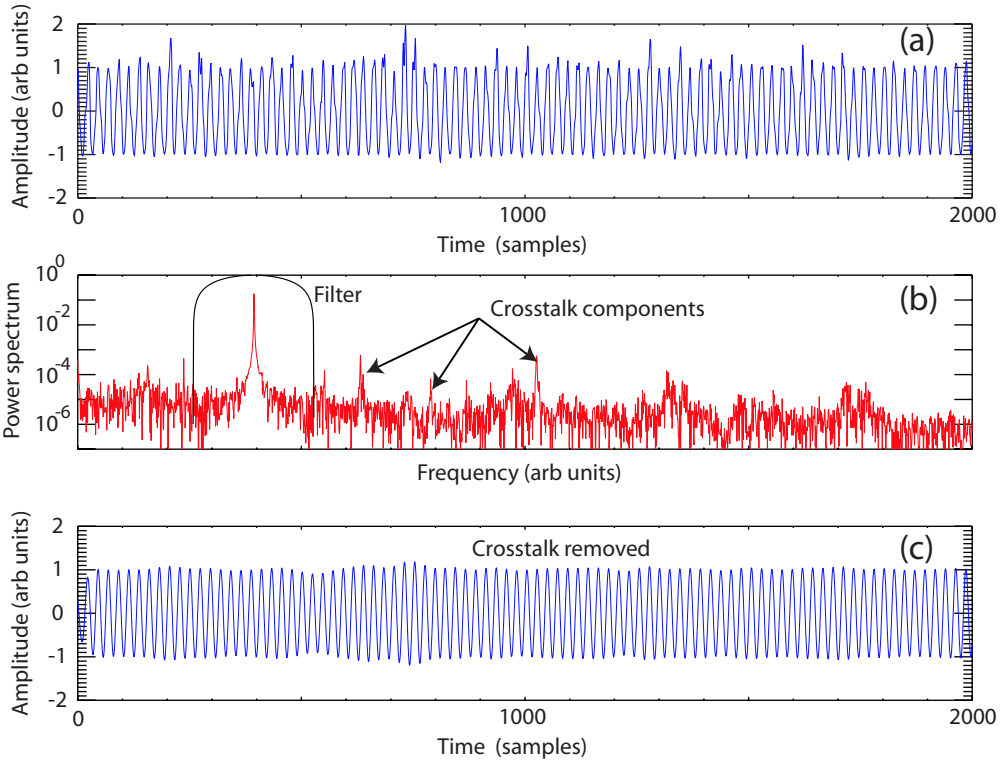
Amplitude (arb units)
2
1
0
-1
-2
0
1000
2000
Time (samples)
(a)
Power spectrum
10^{0}
10^{-2}
10^{-4}
10^{-6}
Filter
Crosstalk components
(b)
Frequency (arb units)
Amplitude (arb units)
Crosstalk removed
(c)
Time (samples)

Fig. 5.

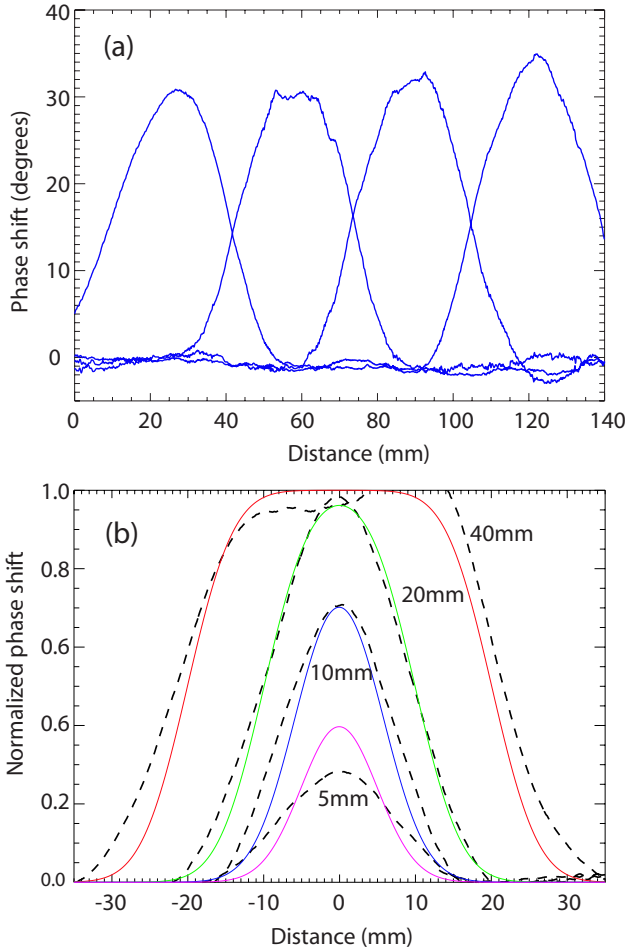
(a)
Phase shift (degrees)
Distance (mm)
(b)
Normalized phase shift
40mm
20mm
10mm
5mm
Distance (mm)

Fig. 6.

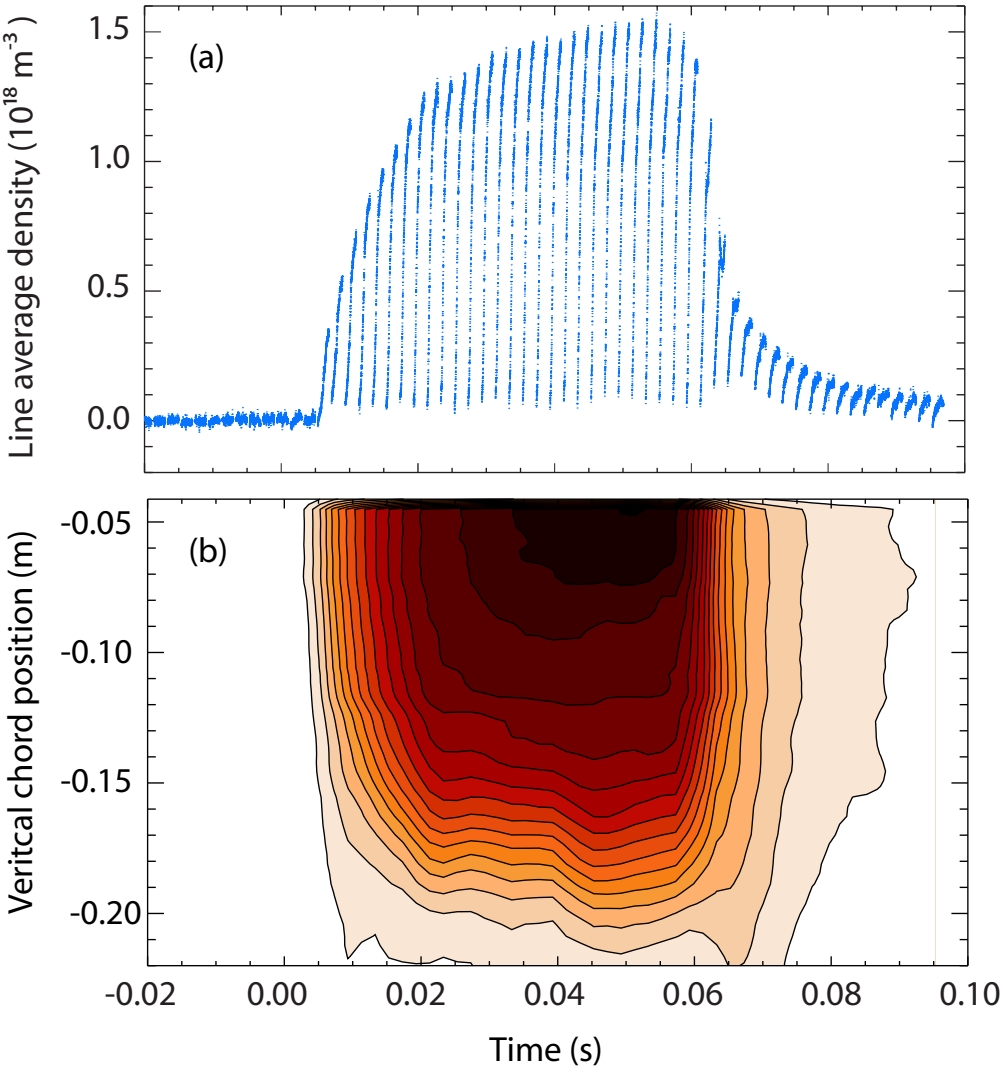
(a)
Line average density (10^{18} m^{-3})
1.5
1.0
0.5
0.0
(b)
Veritcal chord position (m)
-0.05
-0.10
-0.15
-0.20
-0.02
0.00
0.02
0.04
0.06
0.08
0.10
Time (s)

Fig. 7.

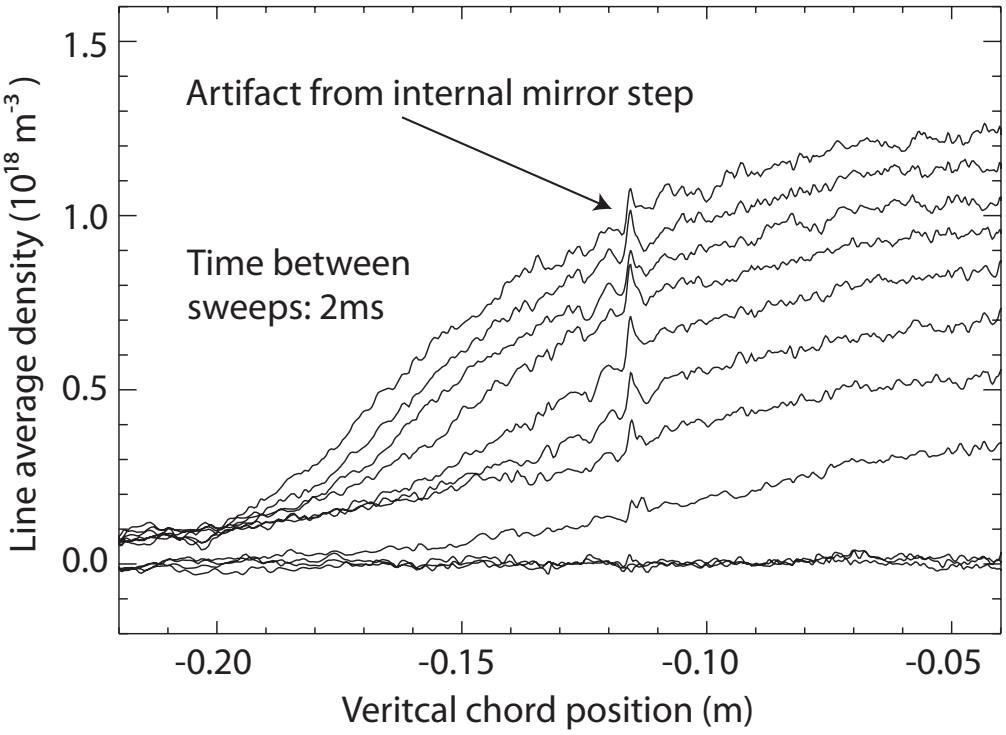
Artifact from internal mirror step
Time between
sweeps: 2ms
Line average density (10^{18} m^{-3})
1.5
1.0
0.5
0.0
-0.20
-0.15
-0.10
-0.05
Veritcal chord position (m)

Fig. 8.

Figure captions

Figure 1. A 3-d Gaussian beam ray trace model of the H-1 scanning interfereometer optical system. Laser radiation incident on the rotating grating is sequentially diffracted through a fan of angles. The beam is collected by monolithic optics mounted on a vertical table, directed into the plasma and returned back along the incident path to processing optics mounted on a horizontal optical table. The grating is illuminated at three positions to allow plasma probing in three directions, two diagonal and one horizontal. The radiation enters the vacuum tank (not shown) via the indicated vacuum port windows.

Figure 2. Raw interferometer projection data for a discharge exhibiting a large scale global instability. Each image shows the temporal evolution (horizontal axis) of the phase shift (radians) for the two diagonal sweeps of the plasma (vertically juxtaposed in the figure).

Figure 3. A schematic diagram of the benchtop interferometer. Test phase objects are placed in the region indicated by the plasma outline. When the wavelength is electronically tuned, the diffraction grating generates a spatial sweep across the plasma region. The optics are arranged so that longer wavelengths probe the plasma edge regions.

Figure 4. (a) Interferogram for full 220-270GHz sweep using a 100Hz linear ramp. (b) Detail of the interferogram during the first 2ms. Note the varying IF frequency and noisy amplitude due to multi-path effects. (c) Power spectrum of the signal in (a). In this instance, approximately 400 waves per sweep gives an IF signal peaked near 40kHz.

Figure 5. (a) The interferogram shown in Fig. 4(a) following amplitude normalization and phase regularization as described in the text. (b) Power spectrum of (a). Note the narrowing (c) Power spectrum of the signal in (a). In this instance, approximately 400 waves per sweep gives an IF signal peaked near 40kHz.

Figure 6. (a) Superimposed phase images of a mylar strip of width 30mm translated across the ELSI field-of-view. (b) Phase images of mylar strips of width 5, 10, 20 and 40mm. The convolution of a Gaussian and a rectangular function (superimposed) compares satisfactorily with the measurements and indicates a spatial resolution of 20mm.

Figure 7. Two representations of demodulated interferometric phase data for a typical 0.5 T minority-heated hydrogen discharge in the standard-magnetic-configuration H-1 heliac. (a) shows the demodulated line average density presented as a raw time series. The multiple stripes correspond to successive sweeps of the BWO beam across the plasma.

In (b) the data have been arranged into an array format indexed according to sweep start time and beam position in the plasma.

Figure 8. Line average plasma density evolution displayed in a single plot as a superposition of successive sweeps. The time between sweeps is 2ms.